

FERMI OBSERVATION OF THE JETS OF THE MICROQUASAR SS433

YI XING¹, ZHONGXIANG WANG¹, XIAO ZHANG², YANG CHEN^{2,3}, V. JITHESH⁴

Draft version January 19, 2022

ABSTRACT

We report our analysis of the data obtained with the Large Area Telescope (LAT) onboard the *Fermi* Gamma-ray Space Telescope (*Fermi*) for the SS 433/W50 region. The total data length is ten years. Different from the previous results reported for this region (for which an old version of database was used), we show that excess emission is detected around the w1 region in the western lobe of the jets from SS 433. The region is bright at X-rays due to the interaction between the jet and the ambient medium. This detection also matches well the recent results of the very-high-energy detection of SS 433/W50 with the High Altitude Water Cherenkov (HAWC). However, the eastern regions that are slightly brighter in HAWC's observation are not detected in the *Fermi* data. Constructing the broad-band spectral energy distribution (SED) for the western region, we compare with the HAWC results for the eastern regions and discuss the possible origin of the emission. A leptonic scenario can provide a fit to the *Fermi* GeV spectrum and HAWC TeV detection, where the former and latter are due to the synchrotron radiation and inverse-Compton process respectively. However, the model can not explain the X-ray and radio emission from the region simultaneously, which thus requires further observational and theoretical studies of the region in order to clarify the reasons.

Subject headings: stars: jets — stars: individual (SS 433) — ISM: supernova remnants

1. INTRODUCTION

SS 433 is probably one of the most well-known sources in the sky that has been extensively studied from radio to very high energies (Fabrika 2004; Bordas et al. 2015; Kar & VERITAS Collaboration 2017; MAGIC Collaboration et al. 2018). This binary contains a compact object and an A-type evolved star (Gies et al. 2002), with an orbital inclination angle of 78° (Eikenberry et al. 2001). Two jets from the compact object point to the east and west directions, interacting with interstellar gas contained in a size of 2° × 1° supernova remnant W50. The distance to SS 433/W50 is 5.5±0.2 kpc (Blundell & Bowler 2004), implying the physical size of 180 pc × 80 pc for W50 (e.g., Goodall et al. 2011). Within W50, different features have been found (for a review, see, e.g., Fabrika 2004). In particular at X-rays, two lobes extending from SS 433 to eastern and western regions of ~60' away are clearly visible (Watson et al. 1983; Brinkmann et al. 1996). Five bright regions (e1–e3 in the eastern lobe and w1 and w2 in the western lobe) were selected for detailed studies, from which these regions were considered as the results of the interaction between the jets and the ambient medium (Safi-Harb & Ögelman 1997; Safi-Harb & Petre 1999; Brinkmann et al. 2007).

Recently the very-high-energy (VHE) emission (at ~20 TeV) from the eastern and western interaction regions has been detected by the High Altitude Water Cherenkov (HAWC) observatory with a significance of

5.4σ (Abeysekara et al. 2018). Modeling of the broad-band spectral energy distribution (SED) of the e1 region indicates a leptonic scenario for the TeV γ-ray emission, in which a single population of electrons with energies up to hundreds of TeVs radiates the synchrotron emission at radio to X-ray frequencies and inverse-Compton (IC) scatter cosmic microwave background (CMB) photons to the observed TeV ones (Abeysekara et al. 2018). The HAWC results have established again, in addition to blazars that are the major class of γ-ray sources in the sky due to their jets, jets associated with Galactic stellar sources are also strong high-energy γ-ray emitters.

However at GeV energies, only excess emission possibly associated with SS 433/W50 was reported from analysis of data obtained with the Large Area Telescope (LAT) onboard the *Fermi* Gamma-ray Space Telescope (*Fermi*; Bordas et al. 2015). This excess γ-ray emission at GeV energies was not clearly associated with the eastern or western interaction regions, different from that indicated by the HAWC detection. Also the LAT data analyzed in Bordas et al. (2015) were obtained during the first 5.5 years of *Fermi* and selected from the P7rev_v15 database. Given these reasons, we re-analyzed the LAT data that were 10 years long and from the latest Pass 8 database. We found different results and report them in this paper. Below we describe the *Fermi* data and source model for analysis in Section 2, and present our analysis and results in Section 3. In Section 4, the results are discussed by considering different physical processes.

2. LAT DATA AND SOURCE MODEL

LAT is a γ-ray imaging instrument scanning the whole sky every three hours (Atwood et al. 2009). In the analysis, we selected 10 years (from 2008-08-04 15:43:36 UTC to 2018-08-05 00:00:00 UTC) LAT events in the 0.1–100 GeV range from the *Fermi* Pass 8 database. A 20° × 20° region centered at the position of SS 433, which is R.A.=19^h11^m49^s.56 and Decl.=+04°58'57".8, were con-

¹ Key Laboratory for Research in Galaxies and Cosmology, Shanghai Astronomical Observatory, Chinese Academy of Sciences, 80 Nandan Road, Shanghai 200030, China

² School of Astronomy & Space Science, Nanjing University, 163 Xinlin Avenue, Nanjing 210023, China

³ Key Laboratory of Modern Astronomy and Astrophysics, Nanjing University, Ministry of Education, China

⁴ Inter-University Centre for Astronomy and Astrophysics, Pune 411 007, India

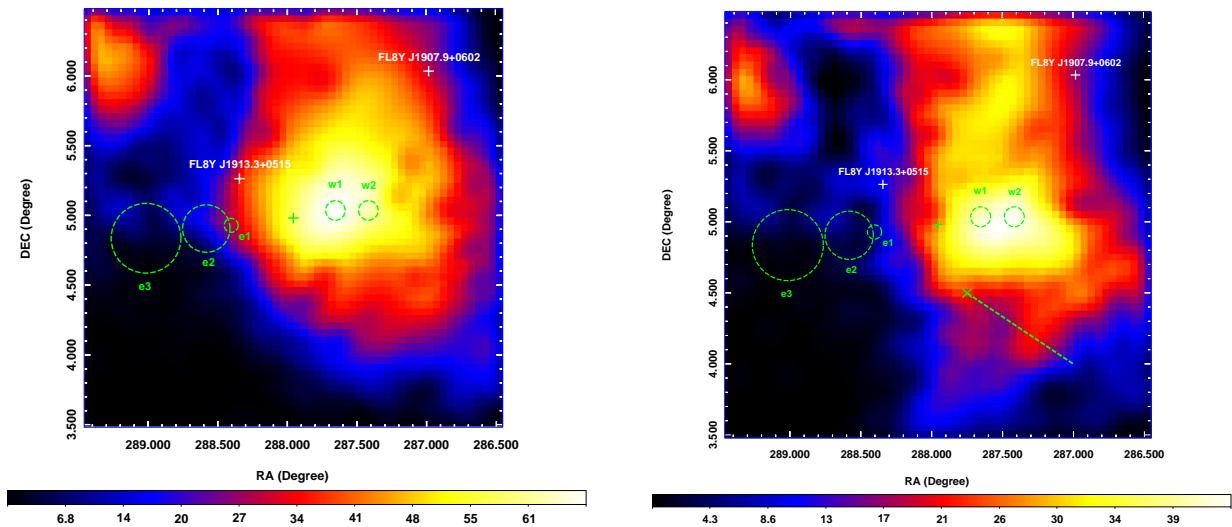


FIG. 1.— $3^\circ \times 3^\circ$ TS maps in 0.3–100 GeV band, extracted using 10-year data (*left* panel) and the data of the same time period as that in Bordas et al. (2015) (*right* panel). The image scale of the maps is $0^\circ 05$ pixel $^{-1}$. TS value ranges are indicated by the color bars. The white plus signs mark the positions of the catalog sources within the region. The green plus signs mark the position of SS 433 and the green circles mark the bright X-ray emission regions of e1–e3, and w1 and w2 defined from X-ray observations (Safi-Harb & Ögelman 1997). In the right panel for a comparison, the high-TS region shown in Figure 1 of Bordas et al. (2015) is indicated by the green cross sign and dashed line, which is far off the w1 and w2 regions.

sidered. We included the LAT events with zenith angles less than 90 degrees to prevent the Earth’s limb contamination, and excluded the events with quality flags of ‘bad’. Both these selections are recommended by the LAT team⁵.

We used the *Fermi* LAT 4-year catalog (3FGL, Acero et al. 2015) and the preliminary LAT 8-year point source list⁶ (FL8Y) to make the source model. Sources within 5 degrees from SS 433 in the FL8Y were included in the source model and their spectral parameters were set free; sources 5–20 degrees away from SS 433 in 3FGL were included with their spectral parameters fixed to the values given in the catalog. The spectral forms of these sources are provided in the two catalogs. We note that FL8Y, released in early 2018, is not encouraged to be used directly and the extended source templates and the Galactic/extragalactic diffuse emission models have not been updated accordingly. Therefore we only used the sources within 5 degrees from SS 433 in FL8Y. In addition, the background Galactic and extragalactic diffuse emission were included by adding the spectral model `gll_iem_v06.fits` and the file `iso_P8R2_SOURCE_V6_v06.txt`, respectively, to the source model. The normalizations of the diffuse components were set as free parameters.

3. DATA ANALYSIS AND RESULTS

3.1. Likelihood Analysis

We performed standard binned likelihood analysis to the LAT data in the 0.3–100 GeV band. The version of the LAT science tools software package used was `v11r5p3`. LAT events below 300 MeV were not included because of the relatively large uncertainties of the instrument response function of the LAT and strong back-

ground emission from the Galactic plane in the low energy range. A $3^\circ \times 3^\circ$ residual Test Statistic (TS) map in 0.3–100 GeV band centered at SS 433 was constructed (left panel of Figure 1), in which all the known sources given in the LAT catalogs were removed. The TS value is a measurement of the fit improvement for including a source at a position in the source model, and is approximately the square of the detection significance of the source (Abdo et al. 2010). It can be seen from the TS map that significant excess emission is detected around the western region w1, as the maximum TS value is ~ 65 around w1 (corresponding to $>7\sigma$ detection significance). In the eastern region, $TS \sim 30$ around e1 but the non-negligible value is likely due to emission in the western region; note that the 68% containment angle of LAT is ~ 2 degrees at 300 MeV. In this analysis, we found photon index $\Gamma = 6.0 \pm 1.3$ and 0.3–100 GeV flux $F_{0.3-100} = 8.4 \pm 1.3 \times 10^{-9}$ photons $s^{-1} cm^{-2}$ for w1, indicating a very steep source spectrum.

Bordas et al. (2015) has reported the detection of γ -ray emission toward the SS 433/W50 region. However in their TS map, the excess emission was in the south west of SS433, far off the w1 and w2 X-ray lobe, and moreover it does not exist in our TS map (see Figure 1). The differences in data analysis between theirs and this work are that they used the `P7rev_v15` database and the time period of the data was the first 5.5 years (MJD 54682.6–56719.4) of the *Fermi* observation. In order to check the reasons for the differences, we repeated their analysis but used the Pass 8 data. The obtained TS map is shown in the right panel of Figure 1. As can be seen, the TS map is nearly the same as that from the 10 years data, while with a maximum value of ~ 40 in the w1 and w2 regions. We therefore conclude that the large differences are likely due to our use of the updated version of the LAT data and instrument response functions, and our results are more consistent with the general features of the region

⁵ <http://fermi.gsfc.nasa.gov/ssc/data/analysis/scitools/>

⁶ <https://fermi.gsfc.nasa.gov/ssc/data/access/lat/fl8y/>

TABLE 1
Fermi LAT FLUX MEASUREMENTS AND UPPER LIMITS OF THE W1
 AND E1 REGIONS

E (GeV)	Band (GeV)	$F/10^{-12}$ (w1) ($\text{erg cm}^{-2} \text{s}^{-1}$)	TS (w1)	$F/10^{-12}$ (e1) ($\text{erg cm}^{-2} \text{s}^{-1}$)	TS (e1)
0.13	0.1–0.2	<6.2	0	<5.5	0
0.24	0.2–0.3	<4.8	0	<8.3	0
0.42	0.3–0.6	3.5 ± 1.7	10	<1.9	0
0.75	0.6–1.0	2.4 ± 0.9	9	<1.7	0
1.33	1.0–1.8	1.2 ± 0.5	5	<0.5	0
2.37	1.8–3.2	<1.2	1	<0.9	0
4.22	3.2–5.6	<1.2	2	<0.9	1
7.50	5.6–10.0	<0.4	0	<0.9	2
13.30	10.0–17.8	<0.2	0	<0.2	0
23.71	17.8–31.6	<1.4	2	<0.4	0
42.17	31.6–56.2	<1.8	2	<0.7	0
74.99	56.2–100.0	<1.1	0	<0.7	0

Note: Flux upper limits are at a 95% confidence level.

obtained at X-ray and TeV energies. Because of these, we do not consider the results in Bordas et al. (2015) in the following analysis and discussion.

In addition, for the purpose of also confirming that there is no detected emission in the eastern region, we performed likelihood analysis to the LAT data of SS 433/W50 by including two point sources at the central positions of e1 and w1. A power law emission was assumed for them. We found that significant γ -ray emission can only be detected at w1 with a TS value of 64, while no significant emission can be detected at e1, as the TS value is ~ 0 . Nearly the same values of photon index and flux in 0.3–100 GeV as the above treating w1 as a single source were obtained.

3.2. Spectral Analysis

We extracted the γ -ray spectrum of the western region by performing maximum likelihood analysis of the LAT data in 12 evenly divided energy bands in logarithm from 0.1 GeV to 100 GeV. The spectral normalizations of the sources within 5 degrees from SS 433 were set as free parameters, and all the other parameters of the sources in the source model were fixed at the values obtained from the above maximum likelihood analysis. A power law model was assumed for the excess emission, with the photon index fixed at 2. The obtained spectrum data are given in Table 1, and the spectrum is shown in Figure 3. Only those spectral data points with their flux values 2 times greater than the flux uncertainties are kept. For other data points, their 95% (2σ) flux upper limits were derived and given. It can be seen that the γ -ray emission from the western region can only be detected in the energy ranges from ~ 300 MeV to 1.8 GeV and the flux decreases steeply, consistent with the above result from the maximum likelihood analysis.

For comparison, we also derived the 95% flux upper limits for the e1 region and provide them in Table 1.

3.3. Variability Analysis

Since SS 433 and W50 region can be variable (Fabrika 2004), we checked the possible variability of the excess emission at the w1 region. Following the procedure given in Nolan et al. (2012), we calculated the variability index TS_{var} in the 0.3–100 GeV energy range. A total of 122 time bins were considered, each containing 30-day data.

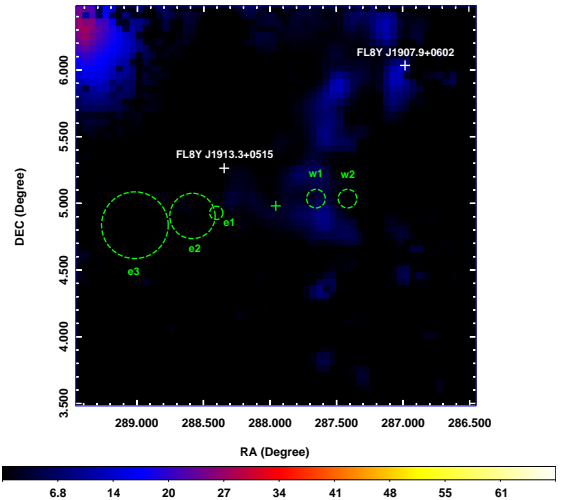


FIG. 2.— $3^\circ \times 3^\circ$ TS residual map in 0.3–100 GeV band, with the excess emission at w1 included as a point source in the source model and removed.

In this case, TS_{var} would be distributed as χ^2 with 121 degrees of freedom if the source flux is constant. We found $\text{TS}_{var} = 103.0$, which is lower than the threshold value of 160.1 for a variable source (at a 99% confidence level; Nolan et al. 2012), indicating that no significant long-term variability was observed in the γ -ray emission.

3.4. Spatial Distribution Analysis

We examined whether the excess emission at the w1 region is a point source or extended. A point source with power-law emission and uniform disk models with power-law emission at the center of the w1 region were used. The searched radius of the uniform disk ranges from 0.1 to 0.5 degree, with a step of 0.1 degree. The TS_{ext} value for the spatial extension was estimated from $-2\log(L_{ps}/L_{disk})$, where L_{ps} and L_{disk} are the maximum likelihood values for the point source and uniform disk model, respectively. TS_{ext} approximately is the square of the detection significance if the excess emission is extended (Lande et al. 2012). In this analysis, TS_{ext} were smaller than 4, indicating that no significant extendedness was present.

In addition, we also tested to include a point source at w1 in the source model, and subtracted it in the resulting TS map. The excess emission was nearly totally removed in the residual TS map (Figure 2). This analysis again indicates that the excess emission can be considered as a point source at w1.

4. DISCUSSION

Analyzing ten years of the *Fermi* LAT Pass 8 data, we found significant γ -ray emission from the western interaction region in W50. The detection significance is $>7\sigma$ in the energy range of 0.3–100 GeV. The location of the emission matches that of the X-ray bright spot and the very recent HAWC detection in the western lobe of W50 (Safi-Harb & Ögelman 1997; Abeysekara et al. 2018), making our results more convincing than that reported in Bordas et al. (2015). No variability or extendedness was found for the emission in our analysis. With

a source distance of 5.5 kpc, the γ -ray luminosity is 1.8×10^{34} erg s $^{-1}$. This luminosity is much lower than the kinetic energy power of the jets, which is at a level of $\sim 10^{39}$ erg s $^{-1}$ (Marshall et al. 2002), indicating that there is sufficient energy to power the γ -ray emission.

The GeV γ -ray spectrum is very steep with $\Gamma \sim 6.0$ from 300 MeV to 1.8 GeV, suggesting that the detected emission should be an edge of an emission component. The flux is higher than that at ~ 20 TeV from the HAWC observation and that of their leptonic model at GeV energies (see Figure 3; Abeysekara et al. 2018), raising a question about how to explain the *Fermi* measurements. The broadband SED for the w1 region is thus constructed by including the HAWC TeV (Abeysekara et al. 2018), X-ray (Safi-Harb & Ögelman 1997), and radio (Geldzahler et al. 1980) measurements. In addition, we also include the VHE upper limits obtained with H.E.S.S. (deeper ones at \sim TeV energies; MAGIC Collaboration et al. 2018).

The leptonic model considered in Abeysekara et al. (2018) to explain the SED of the e1 region obviously cannot fit the detected GeV spectrum, lower by an order of magnitude (see Figure 3). Here we also first construct a leptonic model, in which energetic electrons produce γ -rays by the IC process of scattering the CMB photons, and emissions from radio to X-ray or γ -ray via the synchrotron process. The radiation cooling, mainly due to synchrotron radiation, is included. The current energy distribution of the electrons dN/dE_e is described by $dN/dE_e \propto E_e^{-\alpha_e} \exp(-E_e/E_{c,e})$, where $E_{c,e}$ is the cutoff energy and α_e is the index of the power-law energy distribution. The index becomes $\alpha_e + 1$ if E_e is greater than the break $E_{bre} = 17 (B/5 \mu\text{G})^{-2} (t_{age}/30 \text{ kyr})^{-1}$ TeV (Tanaka et al. 2008). In this case, the GeV and TeV γ -rays can not simultaneously originate from the IC process. In order to match the observed data, the GeV γ -rays should be of synchrotron origin in a magnetic field of $B = 5 \mu\text{G}$, while the TeV γ -rays be contributed by the IC radiation (black curve, Model 1 in the top panel of Figure 3). This requires the injected electron spectrum has a hard index $\alpha_e = 1.5$ and a very large cutoff energy $E_{c,e} = 28$ PeV. The total energy in electrons with energy above 1 GeV is $W_e = 0.7 \times 10^{46}$ erg, which is much lower than the total energy ($\sim 9 \times 10^{51}$ erg) deposited in the jets during the timescale $t_{age} = 30$ kyr. However the model fails to explain the 2.6 GHz radio fluxes detected in the western region (Geldzahler et al. 1980).

A model similar to that in Abeysekara et al. (2018) can be constructed, which can fit the radio measurements (red curve, Model 2 in the top panel Figure 3). In this model, $\alpha_e = 1.9$, $E_{c,e} = 15$ PeV, and $B = 20 \mu\text{G}$. The problem of this model is that it gives an order of magnitude higher X-ray fluxes than the observed. Because latter X-ray observations of the e1 region have shown higher fluxes (Safi-Harb & Petre 1999; Brinkmann et al. 2007) than that reported from the *ROSAT* and *ASCA* observations (Safi-Harb & Ögelman 1997), we search for similar archival X-ray data, but unfortunately there is only one *Chandra* imaging observation of the w2 region (Observation ID is 3843 and the exposure time is 71 ksec). The analysis of the data from this observation gives a 0.6–6 keV luminosity of $\sim 2 \times 10^{34}$ erg s $^{-1}$, only slightly higher than that given in Safi-Harb & Ögelman (1997). There-

fore there is no observational evidence, even indirect one, that would support Model 2 at X-ray energies.

We test to include a hadronic process in which the γ -rays are generated in the collision between relativistic protons and the ambient gas. The protons are also assumed to have a power-law energy distribution $dN/dE_p \propto E_p^{-\alpha_p} \exp(-E_p/3 \text{ PeV})$. We find that this population of protons also fail to simultaneously explain the GeV and TeV γ -ray fluxes. Thus, we add a leptonic component with a fixed spectral index of $\alpha_e = 2.0$ at injection and construct a lepton-hadron hybrid model. In this case, the GeV γ -ray emission is due to the hadronic process with proton index $\alpha_p = 2.9$, and the X-ray and TeV γ -rays are of leptonic origin (black curve, Model 3 in the bottom panel Figure 3), requiring $E_{c,e} = 2.5$ PeV, $B = 5 \mu\text{G}$ and $W_e = 4.8 \times 10^{46}$ erg. This model also fails to explain the radio flux, and has a high total energy in protons $W_p = 3 \times 10^{50} (n/1 \text{ cm}^{-3})^{-1}$ erg, which is comparable to the total jet energy even if the density of the ambient target gas is as high as $\sim 1 \text{ cm}^{-3}$ (see also arguments against a hadronic scenario in Abeysekara et al. 2018). Therefore this hybrid model may be excluded due to these problems.

Finally, we also test to replace the hadronic component in Model 3 with a relativistic thermal electron population (Model 4). This model is based on the results in the particle-in-cell simulations of relativistic shocks (Spitkovsky 2008). In order to explain the resulting particle distribution from the simulations, a model consisting of a relativistic 2D Maxwellian component plus a power-law component with an exponential cutoff is invoked. This model has been applied to pulsar wind nebulae, explaining their broadband spectra (e.g., Slane et al. 2012). In Model 4, we add a relativistic Maxwellian component $dN/dE_e \propto E_e^2 \exp(-E_e/E_{peak})$, where E_{peak} is the peak energy. With this thermal component, we find that the broadband SED of the w1 region can be fitted (red curve in the bottom panel of Figure 3), where reasonable parameters $E_{peak} = 50$ GeV and $W_e^{max} = 6.0 \times 10^{48}$ erg are obtained. However the model has a steeply rising spectrum at radio frequencies. Such a spectrum is not consistent with those obtained in radio observations of W50. The observed spectral indices for W50 at radio frequencies are in a range of ~ 0.4 – 0.7 (e.g., Downes et al. 1986), actually similar to the slope of the leptonic models (e.g., our Model 2).

In a summary, although GeV emission is clearly detected at the western region w1 of SS 433/W50, matching well the X-ray and TeV detections, it is hard to use a simple model to explain the current broadband SED. One possibility is the X-ray flux of the w1 region was underestimated. For the e1 region, a hard X-ray (~ 2 – 100 keV) power-law component has been convincingly detected in different X-ray observations (Safi-Harb & Petre 1999; Brinkmann et al. 2007). A clear detection of a similar component has not been reported for the w1 region, probably due to the lack of X-ray observations. However, it should be noted that the jet emission is likely dominated by a bremsstrahlung component (see, e.g., Migliari et al. 2002), and this thermal component is also probably contained in the X-ray emission from the w1/e1 region (Safi-Harb & Ögelman 1997; Brinkmann et al. 2007), which would reduce the X-ray

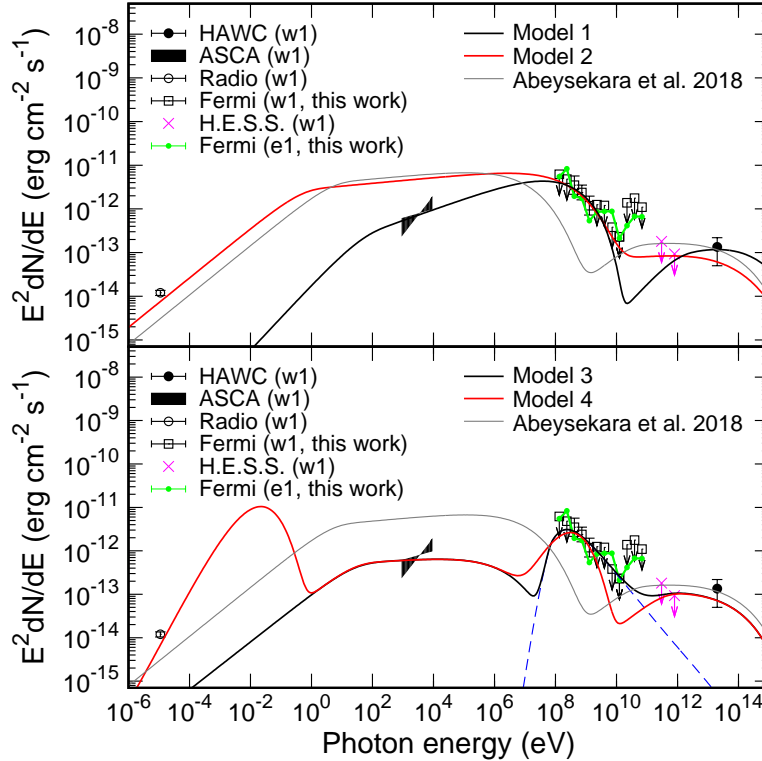


FIG. 3.— *Fermi* LAT spectral energy distribution of the western emission region w1 in W50 (open squares). Also included are the HAWC flux at 20 TeV (black dot; Abeysekara et al. 2018), H.E.S.S. 0.3 and 0.8 TeV upper limits (pink crosses; MAGIC Collaboration et al. 2018), *ROSAT* and *ASCA* flux (black bow-tie; Safi-Harb & Ögelman 1997), and radio fluxes estimated for w1 (open circle; Geldzahler et al. 1980). For comparison, the leptonic model for the eastern emission region e1 given in Abeysekara et al. (2018) is shown as the grey curve and the GeV flux upper limits on the e1 region are shown as a green curve. *Top panel*: our leptonic Model 1 and 2 are indicated by the black and red curves respectively (see Section Discussion for details). *Bottom panel*: the hybrid Model 3 is indicated by the black curve, in which the emission component from the hadronic process is shown as the blue dashed curve, and Model 4 is indicated by the red curve, in which a relativistic Maxwellian component of electrons is included.

flux considered in the SED. In any case to clarify these, further X-ray observations of the w1 region, particularly in the hard X-ray range, are needed. In addition, the TeV fluxes at the w1 and e1 regions are approximately equal (Abeysekara et al. 2018). Except that emission in 0.3–1.8 GeV from the w1 region was weakly detected (with $TS \approx 5-10$), the flux upper limits on the two sides in the other GeV bands are similar (see Table 1 and Figure 3). If we consider that the physical properties of the two lobes of SS 433 should have only small differences, the comparison may suggest that *Fermi* LAT might be close to detecting the e1 region. This possibility can be checked when more LAT data are collected. If this is the case, the model for the e1 region given in Abeysekara et al. (2018) would also need to be modified.

As the current observational results have revealed fine features of a jet interaction region, detailed numerical simulations for investigating the interaction and radiation processes will help. It will identify different populations of high-energy particles. A model consisting of

multiple particle components should definitely be able to explain the SED (for example, our Model 4, although the radio spectrum it produces is steeper than the observed). The possibility raised above about why no GeV emission is seen in the eastern region of SS 433/W50 may also be investigated. We will be able to learn whether this deficit is caused by very detailed differences in the interaction processes.

This research made use of the High Performance Computing Resource in the Core Facility for Advanced Research Computing at Shanghai Astronomical Observatory. This research was supported by the National Program on Key Research and Development Project (Grant No. 2016YFA0400804) and the National Natural Science Foundation of China (U1738131, 11633007). X.Z. and Y.C. acknowledge the supports from the National Program on Key Research and Development Projects 2018YFA0404204, 2017YFA0402600 and 2015CB857100 and from the NSFC under grants 11803011, 11773014 and 11851305.

REFERENCES

- Abdo, A. A., Ackermann, M., Ajello, M., et al. 2010, *ApJS*, 188, 405
 Abeysekara, A. U., Albert, A., Alfaro, R., et al. 2018, *Nature*, 562, 82
 Acero, F., Ackermann, M., Ajello, M., et al. 2015, *ApJS*, 218, 23
 Atwood, W. B., Abdo, A. A., Ackermann, M., et al. 2009, *ApJ*, 697, 1071
 Blundell, K. M., & Bowler, M. G. 2004, *ApJ*, 616, L159
 Bordas, P., Yang, R., Kafexhiu, E., & Aharonian, F. 2015, *ApJ*, 807, L8
 Brinkmann, W., Aschenbach, B., & Kawai, N. 1996, *A&A*, 312, 306
 Brinkmann, W., Pratt, G. W., Rohr, S., Kawai, N., & Burwitz, V. 2007, *A&A*, 463, 611

- Downes, A. J. B., Pauls, T., & Salter, C. J. 1986, *MNRAS*, 218, 393
- Eikenberry, S. S., Cameron, P. B., Fierce, B. W., et al. 2001, *ApJ*, 561, 1027
- Fabrika, S. 2004, *Astrophysics and Space Physics Reviews*, 12, 1
- Geldzahler, B. J., Pauls, T., & Salter, C. J. 1980, *A&A*, 84, 237
- Gies, D. R., Huang, W., & McSwain, M. V. 2002, *ApJ*, 578, L67
- Goodall, P. T., Blundell, K. M., & Bell Burnell, S. J. 2011, *MNRAS*, 414, 2828
- Kar, P., & VERITAS Collaboration. 2017, *International Cosmic Ray Conference*, 35, 713
- Lande, J., Ackermann, M., Allafort, A., et al. 2012, *ApJ*, 756, 5
- MAGIC Collaboration, Ahnen, M. L., Ansoldi, S., et al. 2018, *A&A*, 612, A14
- Marshall, H. L., Canizares, C. R., & Schulz, N. S. 2002, *ApJ*, 564, 941
- Migliaril, S., Fender, R., & Méndez, M. 2002, *Science*, 297, 1673
- Nolan, P. L., Abdo, A. A., Ackermann, M., et al. 2012, *ApJS*, 199, 31
- Safi-Harb, S., & Ögelman, H. 1997, *ApJ*, 483, 868
- Safi-Harb, S., & Petre, R. 1999, *ApJ*, 512, 784
- Slane, P., Hughes, J. P., Temim, T., et al. 2012, *ApJ*, 749, 131
- Spitkovsky, A. 2008, *ApJ*, 682, L5
- Tanaka, T., Uchiyama, Y., Aharonian, F. A., et al. 2008, *ApJ*, 685, 988
- Watson, M. G., Willingale, R., Grindlay, J. E., & Seward, F. D. 1983, *ApJ*, 273, 688